Conformational analysis of proteins with a dual polarisation silicon microring

J-W. Hoste,* S. Werquin, T. Claes, and P. Bienstman

Photonics Research Group (INTEC), Ghent University - imec,
Center for Nano- and Biophotonics (NB-Photonics), Ghent University
Sint-Pietersnieuwstraat 41, 9000 Gent, Belgium

janwillem.hoste@intec.ugent.be

Abstract: Optical microresonator biosensors have proven to be a valid tool to perform affinity analysis of a biological binding event. However, when these microresonators are excited with a single optical mode they can not distinguish between a thin dense layer of biomolecules or a thick sparse layer. This means the sensor is ”blind” to changes in shape of bound biomolecules. We succeeded in exciting a Silicon-on-Insulator (SOI) microring with TE and TM polarisations simultaneously by using an asymmetrical directional coupler and as such were able to seperately determine the thickness and the density (or refractive index) of a bound biolayer. A proof-of-concept is given by determining both parameters of deposited dielectric layers and by analysing the conformational changes of Bovine Serum Albumin (BSA) proteins due to a change in pH of the buffer.

OCIS codes: (130.3120) Integrated optics devices, (140.4780) Optical resonators, (280.1415) Biological sensing and sensors

References and links

1. U.S. Department of Health and Human Services: Food and Drug Administration, “Is it true FDA is approving fewer drugs lately?,” (2011). http://www.fda.gov/AboutFDA/Transparency/Basics/ucm247348.htm.
2. European Federation of Pharmaceutical Industries and Associations, “The pharmaceutical Industry in figures - Edition 2011,” (2011). http://www.efpia.eu/pharmaceutical-industry-figures-edition-2011.
3. U.S. Department of Health and Human Services: Food and Drug Administration, “Innovation or stagnation: Challenge and opportunity on the critical path to new medical products,” (2004). http://www.fda.gov/ScienceResearch/SpecialTopics/CriticalPathInitiative/ucm076689.htm.
4. P.R. Connelly, T.M. Vuong, and M. Murcko, “Getting physical to fix pharma,” Nat. Chem. **3**, 692–695 (2011).
5. E. Reynaud, “Protein misfolding and degenerative diseases,” Nature Education **3**, (2010). http://www.nature.com/scitable/topicpage/protein-misfolding-and-degenerative-diseases-14434929.
6. K. De Vos, J. Girones, T. Claes, Y. De Koninck, S. Popelka, E. Schacht, R. Baets, and P. Bienstman, “Multiplexed antibody detection with an array of silicon-on-insulator microring resonators,” IEEE Photon. J. **1**, 225–235 (2009).
7. M. Iqbal, M. A. Gleeson, B. Spaugh, F. Tybor, W. G. Gunn, M. Hochberg, T. Baehr-jones, R. C. Bailey, and L. C. Gunn, “Label-free biosensor arrays based on silicon ring resonators and high-speed optical scanning instrumentation,” IEEE J. Quantum Electron. **16**, 654–661 (2010).
8. W. Bogaerts, P. De Heyn, T. Van Vaerenbergh, K. De Vos, S. Kumar, T. Claes, P. Dumon, P. Bienstman, D. Van Thourhout, and R. Baets, “Silicon Microring Resonators,” Laser Photon. Rev. **6**, 1–28 (2011).
9. N. J. Freeman, L. L. Peel, M. J. Swann, G. H. Cross, A. Reeves, S. Brand, and J. R. Lu, “Dual-polarisation interferometry: an analytical technique to measure changes in protein structure in real time, to determine the stoichiometry of binding events, and to differentiate between specific and nonspecific interactions,” Anal. Biochem. **329**, 190–198 (2004).
10. S. Ricard-Blum, L. L. Peel, F. Ruggiero, and N. J. Freeman, “Dual polarisation interferometry characterization of carbohydrate-protein interactions,” Anal. Biochem. **352**, 252–259 (2006).

11. F. Bahrami, M. Z. Alam, J. S. Aitchison, and M. Mojahedi, "Dual Polarization Measurements in the Hybrid Plasmonic Biosensors," Plasmonics **8**, 465–473 (2013).
12. Y. Atsumi, D.-X. Xu, A. Delge, J. H. Schmid, M. Vachon, P. Cheben, S. Janz, N. Nishiyama, and S. Arai, "Simultaneous retrieval of fluidic refractive index and surface adsorbed molecular film thickness using silicon wire waveguide biosensors," Opt. Express **20**, 26969–26977 (2012). +
13. S. K. Selvaraja, P. Jaenen, W. Bogaerts, D. Van Thourhout, P. Dumon, and R. Baets, "Fabrication of Photonic Wire and Crystal Circuits in Silicon-on-Insulator Using 193nm Optical Lithography," J. Lightwave Technol. **0**, 1-8 (2009).
14. J. T. Robinson, K. Preston, O. Painter, and M. Lipson, "First-principle derivation of gain in high-index-contrast waveguides.," Opt. Express **16**, . 16659–16669 (2008).
15. K. Okamoto, *Fundamentals of Optical Waveguides* (Academic Press, Burlington, 2008).
16. J. Voros, "The density and refractive index of adsorbing protein layers," Biophys. J. **87**, 553–561 (2004).
17. F. Morichetti, A. Melloni, and M. Martinelli, "Effects of Polarization Rotation in Optical Ring-Resonator-Based Devices," J. Lightwave Technol. **24**, 573–585 (2006).
18. K. E. D. Coan, M. J. Swann, and J. Ottl, "Measurement and differentiation of ligand-induced calmodulin conformations by dual polarization interferometry," Anal. Chem. **84**, 1586–1591 (2012).
19. J. D. Joannopoulos, S. G. Johnson, J. N. Winn, and R. D. Meade, *Photonic Crystals: Molding the Flow of Light* (Princeton University Press, New Jersey, 2008).
20. L. Liu, Y. Ding, K. Yvind, and J. M. Hvam, "Silicon-on-insulator polarization splitting and rotating device for polarization diversity circuits," Opt. Express **19**, 12646–12651 (2011).
21. P. De Heyn, D. Vermeulen, D. Van Thourhout, and G. Roelkens, "Silicon-on-Insulator All-Pass Microring Resonators Using a Polarization Rotating Coupling Section," IEEE Photon. Technol. Lett. **24**, 1176–1178 (2012).
22. N.J. Freeman, L. L. Peel, M. J. Swann, G. H. Cross, A. Reeves, S. Brand, and J. R. Lu, "Real time, high resolution studies of protein adsorption and structure at the solid-liquid interface using dual polarization interferometry," J. Phys.: Condens. Matter **16**, 2493–2496 (2004).
23. P. D. Coffey, M. J. Swann, T. A. Waigh, F. Schedin, and J. R. Lu, "Multiple path length dual polarization interferometry.," Opt. Express **17**, 10959–10969 (2009).
24. K. De Vos, I. Bartolozzi, E. Schacht, P. Bienstman, and R. Baets, "Silicon-on-Insulator microring resonator for sensitive and label-free biosensing.," Opt. Express **15**, 7610–7615 (2007).
25. P. Schiebener, J. Straub, J. M. H. Levelt Sengers, and J. S. Gallagher, "Refractive index of water and steam as function of wavelength, temperature and density," J. Phys. Chem. Ref. Data **19**, 677–717 (1990).
26. T. Peters, "Serum Albumin," Adv. Protein Chem. **37**, 161–245 (1985).
27. S.H. Brorson, "Bovine serum albumin (BSA) as a reagent against non-specific immunogold labeling on LR-White and epoxy resin," Micron **28**, 189–195 (1997).
28. D. C. Carter, and J. X. Ho, "Structure of serum albumin," Adv. Protein Chem. **45**, 153–203 (1994).
29. B. Lillis, M. Manning, H. Berney, E. Hurley, A. Mathewson, and M. M. Sheehan, "Dual polarisation interferometry characterisation of DNA immobilisation and hybridisation detection on a silanised support," Biosens. Bioelectron. **21**, 1459–1467 (2006).
30. S. B. Habib, E. G. Ii, and R. F. Hicks, "Atmospheric oxygen plasma activation of silicon (100) surfaces," J. Vac. Sci. Technol., A **28**, 476–485 (2013).
31. Y. L. Jeyachandran, E. Mielczarski, B. Rai, and J. A. Mielczarski, "Quantitative and qualitative evaluation of adsorption/desorption of bovine serum albumin on hydrophilic and hydrophobic surfaces," Langmuir **25**, 11614–11620 (2009)

1. Introduction

The number of applications to the U.S. Food and Drug Administration (FDA) for new drugs has decreased from 45 in 1996 to 23 in 2010 [1]. Combined with a more than twofold increase of the combined American and European investments in pharmaceutical R&D [2], it is clear that the ruling paradigm for drug research is no longer an efficient one. In the wake of these alarming conclusions, the FDA launched the FDA Critical Path Initiative in 2004 to address the increasing difficulty and unpredictability of medical product development [3]. In a 2011 *Nature Chemistry* Insight [4], the authors state that the reason for the high failure rate in drug development can be found in the lack of appropriate high-throughput tools to study molecular behaviour at an analytical and biophysical level of the drug candidates we produce. This is in contrast to the current, more empirical screening of drug candidates. Specifically, cell metabolism and the failure thereof is often governed by subtle changes in the conformation (i.e. shape) of protagonist proteins or enzymes. Current degenerative diseases (Alzheimer, Huntington, Parkinson,

etc.) that prove difficult to produce effective drugs for, often find their cause in this misfolding of crucial proteins [5].

To accommodate these needs of the pharmaceutical industry, we propose a high-throughput sensor system that can detect conformational changes of proteins. A promising actuator with multiplexing capacities that has received increasing attention during the past few years is an optical microring resonator, designed for the Silicon-on-Insulator (SOI) platform [6, 7]. By putting many of these ring resonator sensors in a dense array on a single chip, it is suitable for high-throughput screening. Detection limits of this platform are ranging from 0.3 $\mathrm{pg/mm^2}$ to 3 $\mathrm{pg/mm^2}$, comparable to surface plasmon resonance sensors [8]. These single-mode sensing systems generally track surface-bound mass as a function of time and as such, provide information on binding dynamics such as binding affinity constants. The perturbation of the effective index (n_{eff}) of this optical mode due a layer of bound molecules is transduced to a measurable entity and is dependent on both the thickness of the layer and its refractive index.

An inherent limitation to all label-free optical sensing technologies that use a single optical mode, is that they can not distinguish between a thin dense biolayer and a thick sparse layer. Hence they only provide information about bound mass or the concentration in a solution. However, by simultaneously determining the thickness(t) and the refractive index(n) of a biolayer, we would obtain information on the contextual conformation of biomolecules. To track both t and n, we propose to excite the microring sensor with two optical modes simultaneously such that we obtain a two-equation system for these two independent variables, as opposed to the single equation we obtain by using only one mode. A similar dual polarisation technique has been used in conjunction with interferometric sensing (DPI) [9], confirming the ability to analyse conformational changes in protein binding events [10]. However, this technique lacks multiplexing abilities and a high-throughput and is suffering from a large footprint, making it less suitable for drug development purposes. Recently this technique has also been applied in the field of plasmonics [11], where higher optical losses are inevitable due to the presence of metal, which limits the limit of detection. In [12] a similar technique based on microring resonators is characterised via simulations, showing its theoretical potential for retrieval of t and n of a bound layer. However, the authors propose a design based on two separate microrings, which has contributions to noise and uncertainty in determining t and n, which are inherently not present in a single microring design, as is proposed in this paper. These noise contributions come from possible variations in binding parameters of a biomolecule layer from one ring to the other, variations in microfluidic conditions and geometrical variations in the microrings due to fabrication tolerances.

2. Working principle and sensor design

2.1. Working principle

The SOI microring is in essence a photonic wire, which is fabricated according to the lithographic process described in [13]. This causes the height of the waveguide to be fixed at 220 nm. All following simulations are done with a height of 220 nm and with an excitation wavelength of 1550 nm. The cross section of this waveguide consists of a silicon rectangle with water cladding on top of a buried oxide layer. This asymmetry causes the microring to be highly birefringent. The two optical modes that excite the microring are the fundamental quasi-TE and the fundamental quasi-TM mode. In the remainder of this text, we shall call these modes TE and TM modes for ease of notation. The resonance wavelength of these two modes in the microring cavity is determined by the effective index of the mode n_{eff}, the length of the cavity L and the order of the mode m:

$$\lambda_{TE} = \frac{L\, n_{eff,TE}}{m} \tag{1}$$

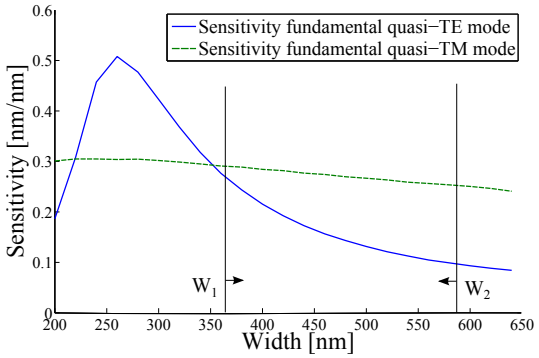

Fig. 1. Sensitivity of the microring resonator to binding of a thin biolayer in water for fundamental quasi-TE mode and fundamental quasi-TM mode, obtained with Fimmwave. The height of the waveguide is fixed at 220 nm and the excitation wavelength is 1550 nm. The region of interest is denoted by W_1 and W_2, where only the fundamental TE and the TM mode are guided

$$\lambda_{TM} = \frac{L\, n_{eff,TM}}{m} \tag{2}$$

Due to birefringence, the field profile of these two modes is different. This profile is translated to a scalar value by means of n_{eff}, which in turn determines the resonance wavelength, causing the modes to resonate at different wavelengths. These modes interrogate the biolayer at the surface by means of their evanescent tail, that penetrates into the cladding of the waveguide. The capturing of biomolecules on the microring surface is reflected by an increase in n_{eff} and thus implies a shift in the resonance wavelength, which is governed by the following equation:

$$\Delta\lambda(n,t) = \frac{\Delta n_{eff}(n,t)\cdot\lambda}{n_g} \tag{3}$$

In this equation $\Delta n_{eff}(n,t)$ represents the change in effective refractive index of a specific mode due to the presence of the protein layer, λ is the resonant wavelength, while $\Delta\lambda(n,t)$ is the shift of this wavelength due to the protein layer. The group index is represented by n_g and its inclusion ensures that first order dispersive effects are taken into account. Figure 1 shows the sensitivity of both modes to a change in layer thickness, expresssed as $\frac{\partial\lambda_{res}}{\partial t}$ as a function of the width of a waveguide, with t the thickness of the biolayer. The width of the microring waveguide should be such, that only the fundamental TE and fundamental TM modes are guided. Simulations with the commercial photonic eigenmode solver Fimmwave show that these conditions are fulfilled when $W > W_1 = 361$ nm and $W < W_2 = 586$ nm. Figure 1 shows that in this region of interest, the TM mode is more sensitive to changes in the thickness of the layer.

The temperature dependence of the TE and TM modes have been determined experimentally and amount to 63 pm/K for the TE and 34 pm/K for the TM mode. The sensitivity to bulk index variations and the penetration depths of both modes have been determined via simulations based on the calibrated waveguide dimensions used in the following BSA experiment. The sensitivity to bulk index variations for the TE mode amounts to 57nm/RIU and 222nm/RIU for the TM mode. The penetration depth is defined as the distance over which the energy density of the modes decrease by a factor 1/e and this amounts to 60 nm for the TE mode and 114 nm for the TM mode.

2.2. *Extraction of (t,n) of the biolayer*

The measurement setup tracks λ_{TE} and λ_{TM} during the experiment. In order to extract (t,n) of the protein layer, we require a set of 2 equations linking the resonance wavelength shifts with these 2 biological parameters:

$$\Delta\lambda_{TE} = f(n,t) \tag{4}$$

$$\Delta\lambda_{TM} = g(n,t) \tag{5}$$

In order to determine f and g, we perform a set of electromagnetic simulations using Fimmwave to calculate these shifts when sweeping over different values of n and t. We subsequently fit an analytical model to these sweeps, which is then used to numerically determine n and t from the measured shifts. We use a similar technique as described in [14] for high-index contrast waveguides as a starting point to obtain this model:

$$\Delta\lambda \propto \frac{\int_{-\infty}^{\infty}\int_{-\infty}^{\infty} n(x,y)\Delta n(x,y)|\mathbf{E}(\mathbf{x},\mathbf{y})|^2 \mathrm{d}x\mathrm{d}y}{\int_{-\infty}^{\infty}\int_{-\infty}^{\infty} n^2(x,y)|\mathbf{E}(\mathbf{x},\mathbf{y})|^2 \mathrm{d}x\mathrm{d}y} \tag{6}$$

where $\Delta n(x,y)$ is the perturbation of the refractive index profile due to the protein layer, such that the denominator is only non-zero in the protein layer. We can solve Eq. (6) using standard waveguide theory [15], but we need to take care not to introduce too many free parameters, as this would result in overfitting to numerical inaccuracies of the mode solver. Therefore we propose the following pseudo 2D analytical model, with n and t the refractive index and thickness of the biolayer and n_b the refractive index of the buffer solution:

$$\Delta\lambda(n,t) = B\,\frac{(n-n_b)nf_p(t,n)}{1+n^2 f_p(t,n)+n_b^2 f_b(t,n)} \tag{7}$$

$$f_p(t,n) = A_{t,p}[1-\exp(-2\delta_p t)] + A_{s,b}[1-\exp(-2\delta_p t)] \tag{8}$$

$$f_b(t,n) = A_{t,b}[\exp(-2\delta_b t)] + A_{s,b}[\exp(-2\delta_b t)] \tag{9}$$

$$\delta_p = k(n_{eff}-n)^{-1/2} \tag{10}$$

$$\delta_b = k(n_{eff}-n_b)^{-1/2} \tag{11}$$

The functions f_p and f_b are the contributions from the protein layer and the buffer cladding. Each of these has a contribution from the top surface, indexed with t, and a contribution from the sidewalls, indexed with s. The normalized amplitudes at the interface between buffer and proteins $A_{t,b}$ and $A_{s,b}$ are determined by $A_{t,p}$ and $A_{s,p}$ using boundary conditions, such that there are 4 parameters to fit per mode: n_{eff},$A_{t,p}$,$A_{s,p}$ and B. To retrieve these parameters, the wavelength shift of both modes is simulated for $t = 0-200$ nm and $\Delta n = 0-0.2$ RIU for a wire waveguide as depicted on Fig. 2(a). We use refractive index unit (RIU) is a unit for the dimensionless refractive index throughout this text. These simulated shifts can then be fit to the model using a least-square metric with physical constraints on the parameters. The results of this fit is shown in Fig. 2(b). An R^2 goodness-of-fit of 0.9998 is obtained, confirming the validity of this model.

2.3. *Influence of noise on measurement accuracy*

With this solving framework we can make an estimate of the error of the system, arising due to noise on the determination of the resonance wavelength. There are various contributions to this wavelength noise from different elements in the measurement setup, such as temperature fluctuations, laser instability while sweeping the wavelength, thermal noise and shot noise from

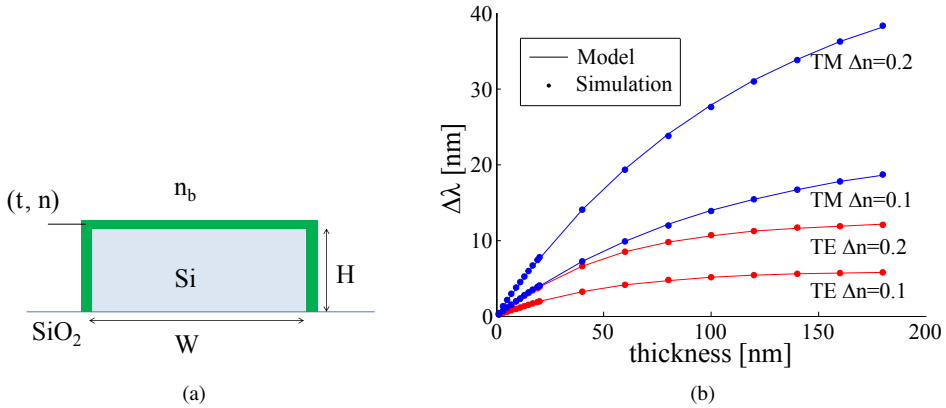

Fig. 2. (a) View of the cross section of the ring waveguide as it is used for simulations. (b) Simulations of the wavelength shifts for both modes in function of the thickness of the protein layer for various refractive indices of this layer. The fitting of this data to the model results in an R^2 value of 0.9998.

the camera capturing the light. To quantify the noise of our system, we have streamed phosphate buffered saline (PBS) at 30 μl/min over the sensor array for 11 minutes, gathering 47 resonant wavelengths per mode. We have quantified the noise as the standard deviation on a linear curve through these measurements, to correct for time dependent linear drift. We have experimentally obtained this noise as 220 fm for the TM mode and 246 fm for the TE mode. This is in good agreement with the noise determined in [7] for a TE mode, where a similar microring and lithographic fabrication process is used. The error in determining (t,n) is calculated as a function of the waveguide width, based on Gaussian wavelength noise with 220 fm standard deviation for both modes. These errors are determined for a protein layer with $n = 1.41 - 1.45$ RIU [16] and $t = 2 - 9$ nm. The average error for a specific waveguide width is depicted on Fig. 3.

Previously, we determined the region of interest for W as 361 nm $< W <$ 586 nm. However, for widths closer to 361 nm, the difference in n_{eff} between both modes decreases such that the mutual coupling increases in the bends of the microring [17]. The reduced width also causes the propagation losses to increase, which results in a decrease of the Q-factor of the cavity. These considerations lead to a choice of W between 460-560 nm. In this region, the average error does not differ much and amounts to 25-30 pm for t and $0.8 \cdot 10^{-3}$-$1.0 \cdot 10^{-3}$ R.I.U. for n. It has been shown that conformational changes of proteins can be measured with a similar resolution in [18].

We have also looked into the possible error that might occur when the coverage at the side of the waveguide is not equal to the coverage at the top. Simulations have shown that assuming unequal coverage either results in unphysical extracted quantities for n and t, or in results which differ by less than 5%. To completely eliminate this uncertainty, we are currently designing a next-generation device where the sidewalls of the ring are embedded in silicon dioxide, such that proteins can only bind to the top.

2.4. Sensor design

In order to excite both polarisations simultaneously we take advantage of the vertical asymmetry of the waveguide. According to [19] the vertical mirror symmetry plane gives rise to two distinct polarisations, one with the electric field confined in this symmetry plane (TE polarisation) and one with the electric field perpendicular to this plane (TM polarisation). In [20] an

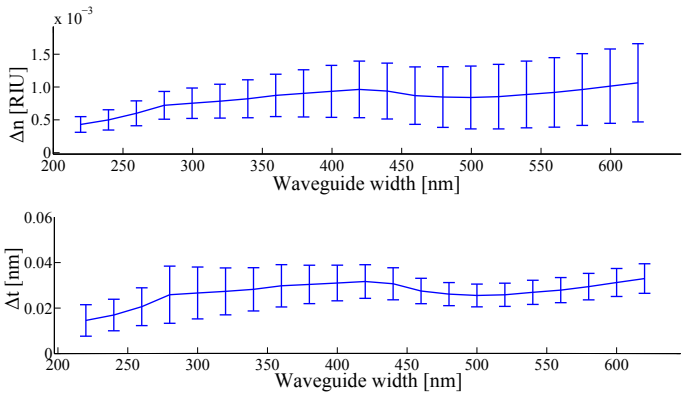

Fig. 3. Mean error on determination of t and n for various widths of the waveguide, with a fixed height of 220 nm.

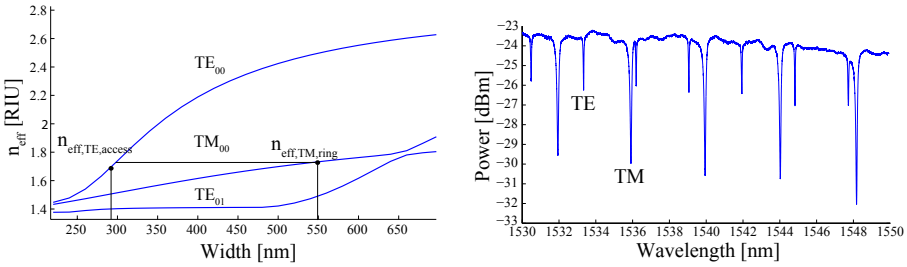

(a) (b)

Fig. 4. (a) Effective index of the first three guided modes for a rectangular waveguide with a height of 220 nm and water cladding. The black lines show the slight phase mismatch for a 550 nm ring waveguide and a 290 nm access waveguide. (b) Measured fiber to fiber spectrum of the microring with water cladding. Both the TE and the TM resonances are visible

asymmetrical directional coupler is suggested that can couple TE light to TM light in an adjacent waveguide by using two waveguides with different widths, such that $n_{eff,TE} \approx n_{eff,TM}$ and the modes are approximately phase-matched. A microring which has an asymmetrical coupling section has been examined in [21], where it was shown that a TE mode in the access waveguide can successfully excite a TM mode in the ring waveguide. However, if the gap in the coupling section is sufficiently small, the TE mode in the access waveguide can also excite the TE mode in the ring waveguide, even though they have a substantial phase mismatch. Indeed, the large modal overlap when the waveguides are very close can compensate for this phase mismatch.

To determine the optimal waveguide dimensions of the ring and the coupling section, we take into account the considerations of the previous section, where we determined that for a microring with a width 460 nm $< W <$ 550 nm we obtained a minimal error on (t,n). For the access waveguide, we need $W >$ 270 nm, such that the fundamental TE mode is still guided by the waveguide, as can be seen on Fig. 1. The waveguide of the microring was designed to have

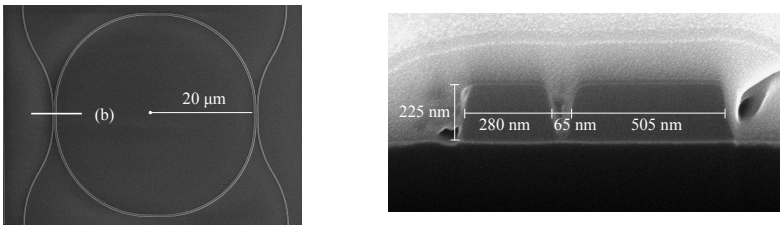

(a) (b)

Fig. 5. SEM image of the microring with access waveguide and a square region where the ions bombarded the coupling section (a). After the ion bombardment, a SEM image of the cross section of the coupling section is taken (b), which shows the waveguide dimensions.

a width of 550 nm, such that with an access waveguide that is 290 nm wide, a small theoretical phase mismatch was achieved between the TE mode of the access waveguide and the TM mode of the ring waveguide of $\Delta n = 0.0481$. On Fig. 4(a), this phase matching is illustrated.

Once the sensor was fabricated, fiber to fiber measurements were performed with water as cladding. The measured spectrum is shown in Fig. 4(b), where the two sets of resonances are visible, each with a different free spectral range (FSR). Figure 5 shows a SEM top view of the microring and a cross section of the coupling section. On the top view of the microring we can see that the access waveguide quickly bends away after the coupling section, such that this section is only 1 μm long. This is done in order to reduce the influence of non-uniform protein binding on the microring behaviour. The cross section shows that for a gap of 65 nm the non-phase-matched coupling of the TE mode of the access waveguide to the TE mode of the ring waveguide can succeed. This gap has been achieved by designing the coupling section with a 120 nm gap on the lithographic mask. Due to optical proximity effects, the gap of the fabricated microring is smaller. Coupling sections with a gap greater than 65 nm have also shown to couple both modes efficiently.

3. Calibration protocol

To extract the thickness of the adsorbed protein layer t and the refractive index of this layer n from ($\Delta\lambda_{TE}$, $\Delta\lambda_{TM}$), we use the extraction scheme as explained in the previous section. There are two caveats, however. In order for the equations to solve to realistic values of t and n, we have to set the width W and height H of the waveguide, as well as the refractive index of the running buffer n_b in the simulations. Due to fabrication tolerances the W and H has to be determined experimentally. A schematic of this calibration protocol is presented in Fig. 6.

Note that W and H are set by the calibration procedure in such a way so as to get accurate results for t and n, and are only abstractions of the true geometry (which could e.g. exhibit slanted sidewalls). W and H could also be obtained from measurements with SEM, but this would not serve as a calibrating mechanism for the simulations. Also, this is a destructive technique, complicating the experiment as well as introducing substantial uncertainty in t and n due to an error of 10 nm on the determination of W and H.

To calibrate the sensor, a three-step sequence of deionised (DI) water, running buffer and DI water is flowed over the sensor prior to the experiment. Each fluid is streamed over the sensor for 10 minutes. When water is flowing over the sensor, the free spectral range (FSR) of both modes is extracted from the spectra. Since DI water has a well-known refractive index, we can use the FSR of the TE and the TM mode to determine W and H [12]. Next, the shift of a resonance wavelength of the TE mode when the fluid is switched from water to buffer

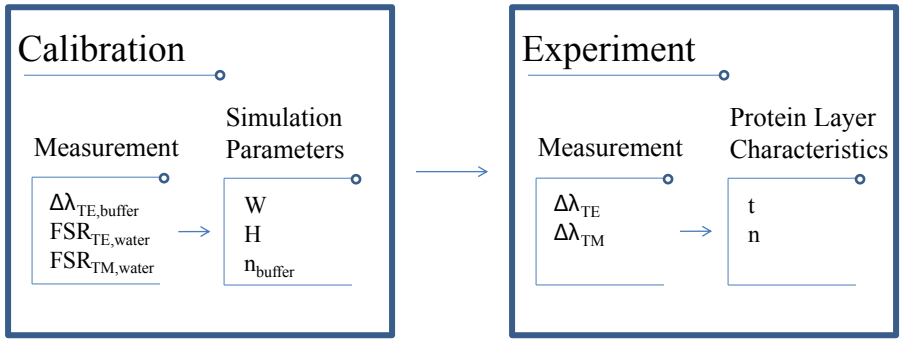

Fig. 6. Schematic diagram of the calibration and the actual experiment. The calibration measurements are done before the measurements for the actual experiment start. They are used to obtain the simulation parameters. These simulations finally determine the model to solve the experimental measurements to the characteristics of the protein layer.

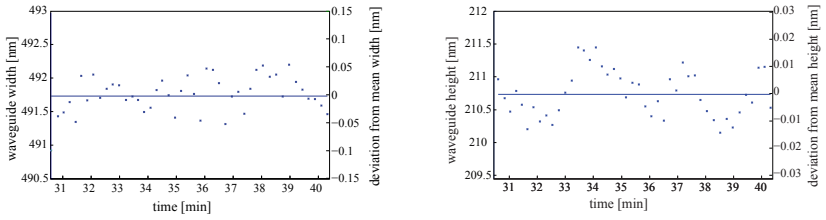

(a) (b)

Fig. 7. By measuring the FSR of both modes during a water phase prior to the following BSA experiment, the (a) width of the ring waveguide was determined with a mean value of 491.7 nm. (b) The height was calculated to be 210.7 nm.

provides the refractive index of the buffer. Directly afterwards, the actual experiment can start. The recorded shifts during the protein experiment can now be adequately solved to the unknown physical quantities t and n. In what follows, the calibration procedure will be explained in detail using the BSA experiment of the next section as numerical example.

To calibrate W and H we use the following equation to obtain the group index (n_g) of both modes from the measured FSR:

$$FSR = \frac{\lambda^2}{n_g L} \tag{12}$$

where L is the length of the microring cavity. Using Fimmwave, we construct surfaces $n_{g,TE}(W,H)$ and $n_{g,TM}(W,H)$ and fit these to a second order model in (W,H). For a parameter space spanning 25 nm for H and 100 nm for W, we obtained a goodness-of-fit of 0.99997 for TE and 0.99991 for TM. This high goodness-of-fit is explained by the high linearity of the group index of the TE mode in W, while the group index of the TM mode is highly linear in H. Physically, these high linearities to either W or H originate from the orthogonality of both modes. The TE mode feels a much higher influence of a change in width, as opposed to a change in height. The opposite conclusions are drawn for the TM mode. When these curves are obtained, the measured FSR of both modes can be used to determine W and H.

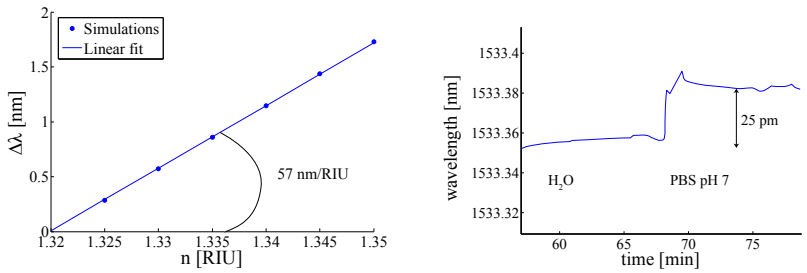

(a) (b)

Fig. 8. (a)Simulation of the wavelength shift of the TE mode in function of the refractive index of a cladding layer with waveguide dimensions of W = 491 nm and H = 210 nm. The wavelength shift is simulated with respect to a buffer with $n_{buff} = 1.32$. (b) Shift of the TE resonance when switching from water to buffer (PBS in this case), as measured in the BSA experiment.

The noise that is present in these measurements propagates to the determination of W and H. Figure 7 shows that the mean width and height of the ring waveguide are $W = 491.7$ and $H = 210.7$. The 3σ deviations during the 10 minutes where water is flown over the sensor amount to 98 pm for W and 26 pm for H. These uncertainties on the simulation parameters imply an uncertainty on the determination of the thickness and refractive index of the protein layer. Both 3σ deviations for W and H were used to calculate a maximum error on thickness of 20 pm and a maximum error on refractive index of 0.62 mRIU. The subsequent BSA experiment was used to estimate these errors. These numbers do not take systematic errors in the fitting procedure into account.

We see that the errors due to calibration uncertainties are almost equal to those due to measurement noise obtained in section 2.3. These results are to be compared to dual polarization interferometry (DPI), which claims a resolution of 100 pm in the context of protein measurements in [22] and a maximum estimated error of 0.003 RIU on refractive index and 25 pm on thickness for measuring dielectric layers of 8 nm height with the enhanced multiple path length DPI [23].

With these calibrated waveguide dimensions, a simulation can be done to estimate the sensitivity of the TE mode to changes in the refractive index of a bulk fluid. In Fig. 8(a) the resonance wavelength shift due to a change in buffer refractive index with respect to water is shown. The high linearity for small changes is visible and amounts to a sensitivity of $\frac{\partial \lambda}{\partial \lambda_{buff}} = 57 \frac{nm}{RIU}$. This is similar to the experimentally verified sensitivity in [24]. The bulk shift from water to buffer (PBS) is 25 pm, as shown on Fig. 8(b). We use the formula derived in [25] to calculate the refractive index of water as 1.3159 at 1532 nm, the average wavelength of the TE and TM mode. The value of n_b is then calculated using the following formula and amounts to 1.3163.

$$n_b = n_{water} + \frac{\Delta\lambda_{TE,b}}{\frac{\partial \lambda_{TE}}{\partial n_b}} \tag{13}$$

4. Proof of concept: dielectric layers and BSA proteins

4.1. Dielectric layers

A first proof of concept is given by measuring the thickness and the refractive index of deposited dielectric layers. Resonance wavelength shifts of the TE and TM modes were measured

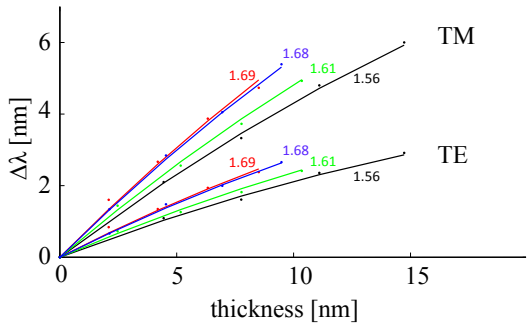

Fig. 9. The dots indicate the measured wavelength shift for TE and TM mode for oxynitride layers with various (t,n) combinations. The solid lines represent the measurements done with an ellipsometer.

for various silicon oxynitride layers, that were deposited with plasma-enhanced chemical vapor deposition. Four different compositions of silicon oxynitride, each with a different refractive index, were deposited on four nominally identical chips. For each composition, the thickness of the layer was increased four times, and the resonance wavelengths were measured in between consecutive depositions. During each transmission measurement, the sensor was covered with water. The refractive index and the thickness of each deposition was measured with a spectroscopic ellipsometer on planar thin films that were deposited in the same run as the layers on the sensor.

On Fig. 9 the measured $\Delta\lambda$ for both modes is shown for these 16 different configurations. Solving the measured shifts results in a standard deviation of 0.2 *RIU* and 1.4 *nm* on the difference between the refractive index and thickness values measured with the ellipsometer and our ring sensor respectively. The wavelength noise on these measurement was as high as 75 pm and 120 pm for the TE and TM modes respectively, probably caused by temperature variations in between the measurements. This high wavelength noise is the root for the high standard deviation on t and n. Nevertheless, the experiment is an indication that the sensor is able to determine thickness and refractive index of a thin layer on top of the waveguide. In experiments with protein binding however, the sensor chip does not leave the setup and as such attains wavelength noise as low as 220 fm, as shown in section 2.3. The next section outlays an example of such an experiment.

4.2. BSA experiment

A BSA molecule can be characterised as a prolate ellipsoid with dimensions $14nm \times 4nm$ [26]. It is often used as a blocking agent in an immunoassay to prevent non-specific binding and adsorption to the surface [27]. The adsorption behaviour of BSA on the silicon surface of the microring is thus crucial to avoid measuring false positives. It is a soft protein, meaning that it can easily change structure and shape depending on the chemical context. In [28] it is shown that it forms reversible conformational isomers in a bulk solution with changing pH. Previous experiments have studied this behaviour in the context of adsorption on a silicon nitride surface with the DPI technique [22] by dissolving the BSA molecules in a PBS buffer and streaming

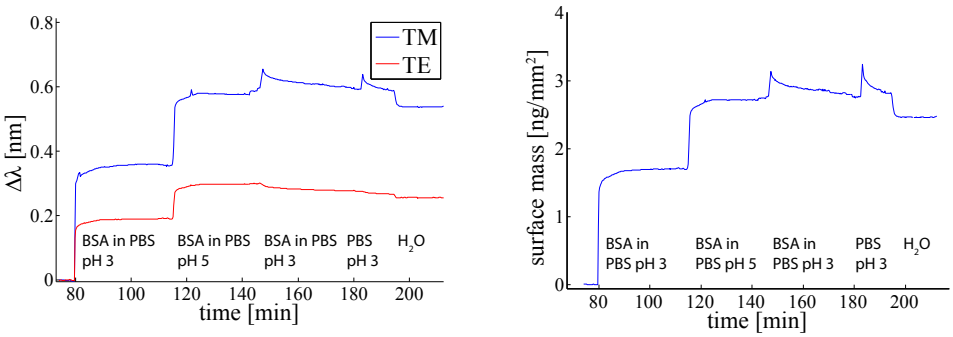

(a) (b)

Fig. 10. (a) Resonance wavelength shift of the fundamental TE mode and fundamental TM mode of the BSA experiment in function of time.(b) Adsorbed mass ng/mm^2 of BSA molecules to the silicon surface.

this solution over the sensor. They have shown that the adsorption is reduced at pH 3 with respect to pH 5 [22]. As a proof-of-concept we record the (t,n) profile of the adsorption of the BSA molecule to the silicon surface, while changing the pH value of the buffer. This way, we show that the dual polarisation microring sensor is capable of recording conformational changes.

A 2mM phosphate buffer solution (PBS) was prepared with pH 5 and 3, to which BSA molecules were added until a concentration of 0.1 mg/ml was attained. Some PBS with pH 3 was left as running buffer. The laser was swept continuously from 1529-1543 nm, at a sweep rate of 2 nm/sec. The captured spectrum consisted of 4 fundamental TE modes and 3 fundamental TM modes. All the reagents were streamed over the chip at a rate of 30 μl/min. After streaming the calibration fluids as described in section 3, the experiment started by streaming PBS for 10 min. The flow was switched from running buffer to BSA in PBS at pH 3 for 10 minutes, followed by a 20 min incubation time. Then, we switched the flow to BSA in PBS at pH 5 for 10 minutes, after which an incubation time of 20 min followed. Eventually the flow was switched back to BSA in PBS at pH 3 for 10 minutes, followed by a 20 min incubation time, before the flow was switched to running buffer and eventually water. The captured resonance wavelengths of a TE and a TM mode are shown on Fig. 10(a).

The calibration protocol is applied to obtain W,H and n_{PBS} and consequently the methods described in section 2.2 are applied to calculate the thickness and the refractive index of the adsorbed BSA layer during the experiment, as shown on Fig. 11. With the commonly used density of proteins of $\rho_{mol} = 1.35$ g/cm^3, the adsorbed mass can be obtained from n by using the following formula [29]:

$$\rho = \rho_{mol} \frac{n - n_B}{n_{mol} - n_B} \tag{14}$$

with n_B the refractive index of the buffer and n_{mol} the refractive index of the dry molecule, which is 1.45 for a wide class of proteins. The adsorbed mass, illustrated in Fig. 10(b), can be calculated as

$$M = \rho\, t \tag{15}$$

A comparison between the measurements made with DPI on silicon nitride [22] and with the SOI microring as described here, is presented in Table 1. The values for pH 3 are referring to the first streaming of BSA in PBS at pH 3. For the thickness of the protein layer we see a

Table 1. Comparison of the thickness, refractive index and adsorbed mass between the technique described in this paper (SOI Microring) and the silicon nitride dual polarisation interferometric (DPI) technique used in [22].

	t pH 3	n pH 3	M pH 3	t pH 5	n pH 5	M pH 5
Microring	1.4 nm	1.433	1.70 ng/mm^2	3.0 nm	1.407	2.72 ng/mm^2
DPI	0.8 nm	1.445	0.48 ng/mm^2	4.8 nm	1.425	2.11 ng/mm^2

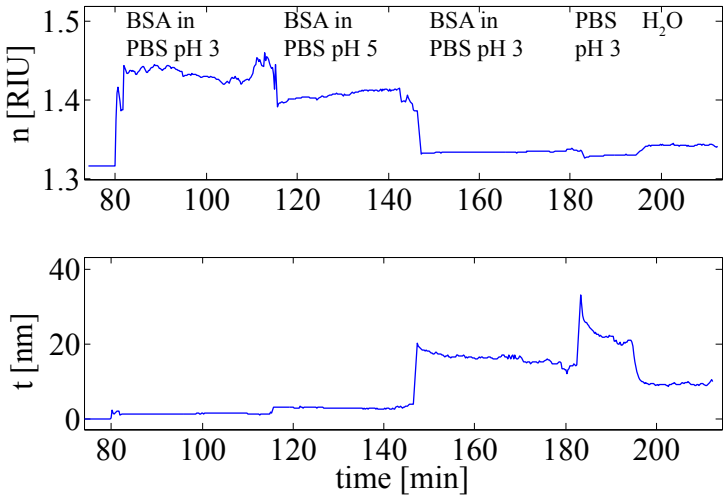

Fig. 11. Thickness and refractive index profile of the layer consisting of adsorbed BSA molecules.

difference smaller than 1 nm for pH 3 and about 2 nm for pH 5. For the refractive indices there is a difference of 0.02 RIU. The general trend of an increased adsorbed mass at pH 5 compared to pH 3 is confirmed, albeit with a higher adsorbed mass on silicon compared to silicon nitride. The increased adsorbed mass at pH 5 with respect to pH 3 can be explained by the fact that BSA molecules are close to their isoelectric point for pH 5, meaning that the molecules are almost free of charge such that they do not repel each other. This in contrast to BSA molecules at pH 3, which have a positive charge. This also explains the slow contracting that is occurring during pH 5. This can be seen at Fig. 11, where the thickness decreases slightly during pH 5 and the refractive index, or density, rises with a similar small slope. At a pH value of 3 the BSA molecules are positively charged, while the silicon surface is negatively charged. Thus, the molecules tend to make as much contact as possible with the surface due to electrostatic attraction, forming a thin, yet dense layer. When the pH value rises from 3 to 5, the BSA molecules become neutral and thus they lose this strong electrostatic attraction. They thus form a thicker layer which is albeit less dense due to the expansion of the molecules.

Although it is clear that the trends of the adsorption behaviour are the same for both techniques, there are small differences in t, n and M of the adsorbed BSA layer as seen in Table 1. We can explain these by looking at the different surfaces used in both techniques. To bond the silicon chip with a fluidic cell, we activated the silicon chip with an oxygen plasma, thus creating an extremely hydrophilic surface [30]. In comparison, the silicon nitride surface of the

DPI technique is more hydrophobic. This different hydrophilicity has a great influence on the conformation of adsorption of BSA molecules [31]. Another observation that is being made in [31] is that the adsorption of BSA saturates at only 50% surface coverage for hydrophobic surfaces, while it can amount to 95% for hydrophilic surfaces. This is confirmed by the higher adsorbed mass with the SOI microring technique compared to the adsorbed mass with the silicon nitride DPI technique. Finally the authors of [31] also describe the inability to wash off adsorbed BSA molecules on a hydrophilic surface. This explains the non-reversible nature of this experiment: there is no decrease in mass when the fluid is switched back from pH 5 to pH 3. The BSA molecules become positively charged when the pH drops back to 3, such that they feel the electrostatic repulsion of neighbouring molecules, yet they can not desorb easily. At this stage we see a drop in refractive index to 1.335 , accompanied by an increase in thickness to 19 nm, which saturates to 14 nm, which is exactly the long side of the BSA molecules in bulk solution. This suggests that the BSA molecules turn upright due to the increased repulsion, such that they are dangling in the buffer, explaining the very thick and sparse layer. Since the BSA molecules have a pronounced denaturation during adsorption to hydropilic surfaces, they can be longer than in a bulk solution. The experimental observation of the inability to wash off the BSA molecules on a plasma-treated silicon surface under various conditions is important in an immunoassay as it prevents the blocking step to degrade in the washing steps of the immunoassay itself.

5. Conclusion

An optical biosensor that consists of a microring resonator based on the Silicon-on-Insulator platform and that is excited by two polarisations simultaneously has been presented. Tracking the resonance wavelength of a TE and a TM mode allows to calculate the thickness and the refractive index of a small (protein) layer, bound to the surface. For this, a calibration procedure and theoretical models have been presented. This sensor has been fabricated and as a proof of concept the refractive index and the thickness of adsorbed silicon oxynitride layers have been determined. To show the potential of this sensor for conformational analysis of proteins, the adsorption mechanisms of bovine serum albumin molecules on a silicon surface have been investigated. The results of these experiments correlate well with literature.